SCIENTIFIC REPORTS

OPEN

SUBJECT AREAS:
MATERIALS FOR ENERGY AND CATALYSIS
ELECTROCHEMISTRY

Received
17 March 2014

Accepted
16 June 2014

Published
8 July 2014

Correspondence and requests for materials should be addressed to Y.S.J. (ysjung@unist.ac.kr)

Interfacial Architecture for Extra Li^+ Storage in All-Solid-State Lithium Batteries

Bum Ryong Shin[1], Young Jin Nam[1], Jin Wook Kim[1], Young-Gi Lee[2] & Yoon Seok Jung[1]

[1]School of Energy and Chemical Engineering, Department of Energy Engineering, Ulsan National Institute of Science and Technology (UNIST), Ulsan, 689-798, Korea, [2]Power Control Device Research Team, Electronics and Telecommunications Research Institute (ETRI), 218, Gajeongno, Yuseong-gu, Daejeon, 305-700, Korea.

The performance of nanocomposite electrodes prepared by controlled ball-milling of TiS_2 and a Li_2S–P_2S_5 solid electrolyte (SE) for all-solid-state lithium batteries is investigated, focusing on the evolution of the microstructure. Compared to the manually mixed electrodes, the ball-milled electrodes exhibit abnormally increased first-charge capacities of 416 mA h g^{-1} and 837 mA h g^{-1} in the voltage ranges 1.5–3.0 V and 1.0–3.0 V, respectively, at 50 mA g^{-1} and 30°C. The ball-milled electrodes also show excellent capacity retention of 95% in the 1.5–3.0 V range after 60 cycles as compared to the manually mixed electrodes. More importantly, a variety of characterization techniques show that the origin of the extra Li^+ storage is associated with an amorphous Li–Ti–P–S phase formed during the controlled ball-milling process.

Demands for large-scale rechargeable batteries for electric vehicles (EVs) and energy storage systems are increasing interest in ultimately safe all-solid-state lithium batteries (ASSLBs) using inorganic solid electrolytes (SEs)[1–4]. A composite-type ASSLB, in which the electrode layer has a three-dimensional (3D) structure consisting of particulate mixtures of active materials, SEs, and conductive additives, has attracted much attention as being close to commercialization in the future[5]. To date, promising performance has been demonstrated mostly by composite-type all-solid-state rechargeable batteries with sulfide SEs[2,3], which is attributed to several important characteristics. First, sulfide SEs with high ionic conductivities of 10^{-3}–10^{-2} S cm^{-1} have been developed, including a thio-lithium superionic conductor (thio-LISICON, $Li_{3.25}Ge_{0.25}P_{0.75}S_4$, 2.2 × 10^{-3} S cm^{-1})[6], glass–ceramic $70Li_2S$–$30P_2S_5$ ($Li_7P_3S_{11}$, 3.2 × 10^{-3} S cm^{-1})[7], and $Li_{10}GeP_2S_{12}$ (1.2 × 10^{-2} S cm^{-1})[2]. Second, ductile sulfide SEs can make intimate contact with active particles, providing good ionic conduction pathways by simple cold pressing[3,8]. This is in contrast to "hard" oxide SEs such as garnet-type $Li_7La_3Zr_2O_{12}$[9]. Electrodes using the oxide SEs need to be sintered in order to make two-dimensional (2D) contacts with active particles rather than point contacts, which inevitably forms an undesirable Li^+ ion barrier layer at the interface, resulting in failure during operation of the battery[10,11].

In order to develop ASSLBs that can eventually compete with conventional lithium-ion batteries, several issues should be addressed. First, because the Ge included in LGPS is expensive, highly conductive alternative SEs should be further developed. Second, without a metal oxide coating such as $Li_4Ti_5O_{12}$[12], $LiNbO_3$[2], Li–Si–O[13], or Al_2O_3[14], sulfide SEs are not compatible with conventional layered or spinel oxide cathodes such as Li_xMO_2 (M = Co, Ni, Mn). This can be attributed to the intrinsically low oxidation onset potential of the sulfide SEs (~3 V)[15] and incompatibility between $LiMO_2$ and the sulfides[12,16]. Third, 3D design of the electrode layer is critical for the performance of ASSLBs. In the configuration of lithium-ion batteries, numerous studies on the design of the electrode have focused on how to achieve good electronic conduction pathways, short Li-ion diffusion pathways in active particles by downsizing, and so on[4]. These approaches are based on the fact that liquid electrolytes can readily wet the active materials, and thus transport of Li^+ ions in LEs is much faster than solid-state Li^+ ion diffusion and electronic conduction within the active materials. In ASSLBs, however, the solid nature of SEs adds one more important consideration in designing composite electrodes, which is ionic conduction through the percolated SE particles and at the interfaces between active materials and SEs. More creative approaches to distributing SEs homogeneously in order to ensure good percolation and favorable contact with active particles will advance the success of ASSLBs. For example, adding a thin SE coating by laser evaporation has been demonstrated to improve the performance of ASSLBs significantly[8,17].

In choosing alternative cathode materials for ASSLBs, elemental sulfur has been considered due to its high theoretical capacity (1675 mA h g^{-1})[18,19]. Sulfur also does not suffer from polysulfide dissolution with SEs[18–21]. However, the extremely low conductivity and severe volume change during charge and discharge (theoretically ~ 179% for $S + 2Li^+ + 2e^- \leftrightarrow Li_2S$) are still problematic. Although extensive research efforts focused on inter-

calation/deintercalation of Li in the layered transition metal dichalcogenides in the 1970s[22], transition metal sulfides were eventually not commercialized. They operated at lower voltages than the competing Li_xMO_2, initially required a lithiated anode, had a compatibility issue with the liquid electrolytes, and so on[23,24]. Conversely, when it comes to ASSLBs using sulfide SEs, the transition metal sulfides can be attractive candidates because their mild operating voltages (less than ~3 V) are suitable for sulfide SEs, they have potentially good compatibility with sulfide SEs, and they exhibit a highly reversible intercalation reaction with Li. In particular, promising performance of ASSLBs has been reported using TiS_2[25,26], which can be attributed to the aforementioned advantages and metallic nature of TiS_2. One of the remaining challenges for using transition metal sulfides for ASSLBs is that their limited capacity is not enough to compensate for the low working voltage. In a previous report by Lee et al., decreasing the particle size of TiS_2 from ~10 to 0.1 μm by ball-milling was demonstrated to increase the power density of ASSLBs[25]. The underlying mechanism is thought to be associated with the shortened Li^+ ion diffusion length in the TiS_2 and the increased interfacial contact area. Considering that the SEs are particles, there should be opportunities for further improvements by size control of the SE and better mixing of SE and TiS_2 in terms of homogeneous distribution and intimate contact. Some control of the TiS_2 and SE interface also may affect the electrochemical behavior.

In this study, we demonstrate an abnormally increased capacity without loss of the rate capability by using a scalable simple mechano-chemical process for fabricating an interfacial architecture consisting of TiS_2 and Li_2S–P_2S_5 SE for ASSLBs. Combined analyses by *ex situ* X-ray diffraction (XRD), field-emission scanning electron microscopy (FESEM), detailed high-resolution transmission electron microscopy (HRTEM) with energy dispersive spectroscopy (EDS), *ex situ* Raman spectroscopy, *ex situ* X-ray photoelectron spectroscopy (XPS), and various other electrochemical techniques show how the microstructure of electrodes results in the extra capacity while retaining good electronic and ionic conduction pathways.

Results and Discussion

We prepared an electrode by controlled ball-milling of both TiS_2 and SE particles, denoted as BMe (ball-milled electrode). Because TiS_2 is metallic, carbon additives are not needed. As a counter reference, another electrode was prepared by manual mixing of TiS_2 and SE particles, denoted as HMe (hand-mixed electrode). A Li_3PS_4 (or $75Li_2S$–$25P_2S_5$) glass-ceramic SE with a conductivity of 1.0×10^{-3} S cm^{-1} at 30°C was selected because it is free from unreacted Li_2S, which may disturb the interpretation of the capacity (Figure S1 (Supplementary Information)).

Figure 1a shows the FESEM images of the HMe and BMe powders and their corresponding elemental maps of Ti (red) and P (green) with EDS. As seen in the image of HMe, the regions of TiS_2 and SE particles with sizes of a few to tens of micrometers are clearly separated, whereas there is no clear separation observed in the BMe images. The particles in the BMe are much smaller than those in the HMe. Also, the signals of both Ti and P are homogeneously distributed in BMe, suggesting better mixing and more favorable contacts between TiS_2 and SEs. Figure 1b compares the XRD patterns of HMe and BMe. Three features are noticeable in the BMe as compared to the HMe. First, the intensity of the main peaks for TiS_2 is significantly decreased. This result indicates not only reduced crystallinity[25] but also a possible consumption of TiS_2 by the reaction between TiS_2 and Li_3PS_4 SE during ball-milling. The crystallite size in the [001] direction using the Scherrer equation is ~37 nm[27]. Second, the characteristic peaks for the SEs (the carat marks, ^) are still visible, implying that the ionic conduction pathways are intact. The slightly decreased intensities of the SE peaks (denoted as '^' in the inset) in the BMe supports the possible reaction between TiS_2 and

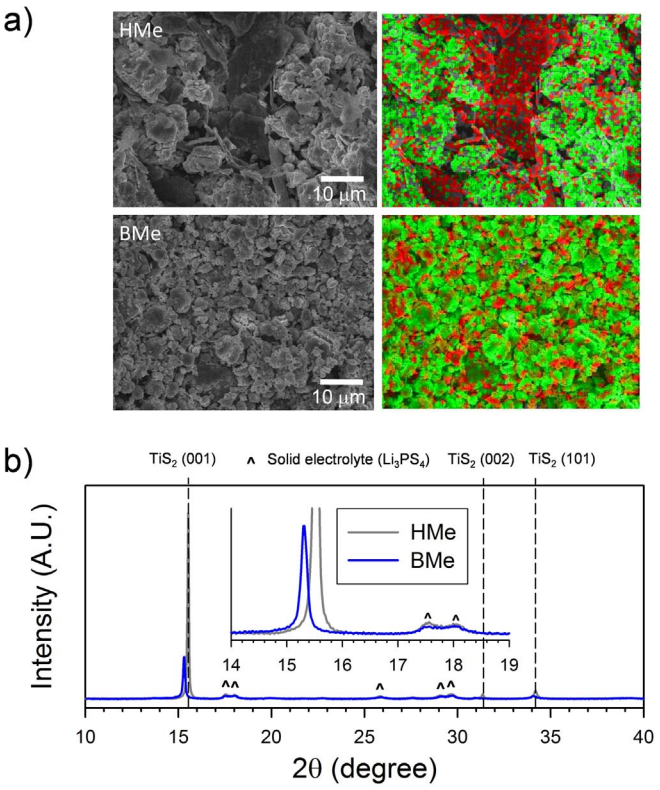

Figure 1 | (a) FESEM images and corresponding elemental maps with EDS (red: Ti, green: P) of electrode powders prepared by hand-mixing (HMe) and by ball-milling (BMe) TiS_2 and solid electrolyte (SE). (b) XRD patterns of HMe and BMe.

SE during the ball-milling process. Third, the position of the TiS_2 peaks after ball-milling is negatively shifted, indicating partial lithiation of TiS_2[28,29]. At this point, the source of the lithium should be the SE, suggesting that there must be some reaction between TiS_2 and SE during ball-milling.

The all-solid-state cells of TiS_2–SE/SE/$Li_{0.5}In$ employing HMe and BMe were cycled between 1.5 and 3.0 V and between 1.0 and 3.0 V at 50 mA g^{-1} at 30°C. The capacities are based on the weight of TiS_2. The first two discharge–charge voltage profiles are represented in Figure 2. Two electrodes of BMe with ball-milling times of 3 and 9 min are also compared. The first discharge capacity of HMe almost reaches the theoretical capacity of TiS_2 (239 mA h g^{-1}, $TiS_2 + Li^+ + e^- \leftrightarrow LiTiS_2$) between 1.5 and 3.0 V in Figure 2a. After ball-milling for 3 min (Figure 2b), a slight increase in capacity and a change of voltage shapes are seen. Upon further ball-milling for 9 min (Figure 2c), the changes are significant. Although the first discharge capacity is almost the same, the electrode surprisingly exhibited significantly increased capacity at the first charge and during the subsequent cycle. Also, the voltage curves become smoother. Table 1 summarizes the first cycle capacities and Coulombic efficiency of HMe and BMe. When ball-milling is performed for 9 min, the first charge capacity is almost doubled from 220 mA h g^{-1} to 416 mA h g^{-1}, which far exceeds the theoretical capacity. Also, the couloumbic efficiency is increased from 93% to 158%. A couloumbic efficiency of more than 100% indicates that the amount of extracted lithium is more than the inserted amount. The BMe with the 9-min ball-milling (denoted as BMe-9-min), which is subjected to charge (delithiation) first, as seen in the inset in Figure 2c, affords 151 mA h g^{-1}. This value corresponds perfectly with the difference between the first charge capacity and discharge capacity (416 − 263 = 153 mA h g^{-1}) of the same cell under normal cycling conditions (discharge or lithiation first). From the position of the (001) peak of Li_xTiS_2

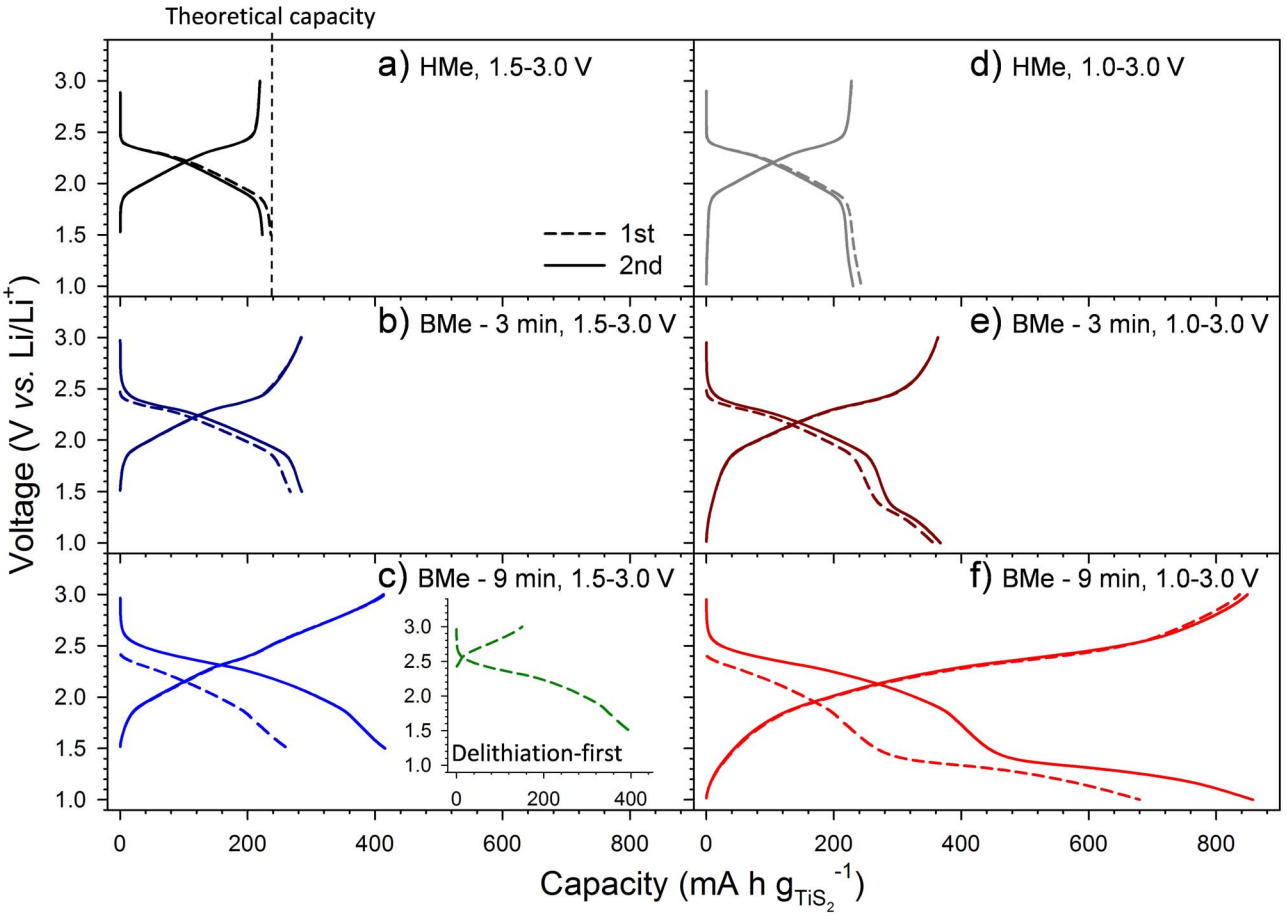

Figure 2 | First two discharge–charge voltage profiles of HMe and BMe at 50 mA g^{-1}. Left and right column show the curves between 1.5–3.0 and 1.0–3.0 V, respectively. The inset in c shows the first-cycle voltage profiles when charge (delithiation) is carried out first.

(15.3°) in Figure 1b, *d* spacing value is 5.78 Å. The *ex situ* XRD results of the HMe cell in Figure S2 describes the relationship between the degree of lithiation of TiS_2 (x in Li_xTiS_2) and *d*[28]. When 5.78 Å of *d* is applied to the fitted curve in Figure S2c, x in Li_xTiS_2 for the BMe sample becomes 0.05. Complete delithiation from $Li_{0.05}TiS_2$, however, accounts for only ~12 mA h g^{-1} at maximum, which is far lower than the first charge capacity of 151 mA h g^{-1} shown in the inset of Figure 2c. Also, the origin of the abnormally increased reversible capacity of 177 mA h g^{-1} (first charge capacity − theoretical capacity = 416 − 239) of the BMe-9-min cell as compared to that of HMe is questionable, which will be discussed in detail later.

Decreasing the lower cutoff voltage down to 1.0 V, the changes in electrochemical behavior as a function of ball-milling time is more dramatic. For HMe, no noticeable reaction occurs in the 1.0–1.5 V range (Figure 2d). As the ball-milling time increases (Figures 2e and 2f), however, a new long plateau at ~1.3 V develops, resulting in a significant increase in the reversible capacity up to ~840 mA h g^{-1}.

Table 1 | Electrochemical results HMe and BMe electrodes

Electrode	First cycle capacity (mA h g^{-1})		Coulombic efficiency (%)
	Discharge	Charge	
HMe	237	220	93
BMe - 3 min	267	285	107
BMe - 9 min	263	416	158
BMe - 9 min charge-first	-	151	-

This value is ~3.6 times higher than the theoretical capacity of TiS_2. Another counter reference electrode was prepared by manually mixing ball-milled TiS_2 for 9 min and SE particles, denoted as HMe-BM-TiS_2. The XRD pattern of HMe-BM-TiS_2 exhibited a lower intensity for TiS_2 but no shift in peak positions (Figure S3a). Also, the capacity is almost the same as that of HMe (Figure S3b). This control experiment strongly suggests that some reaction between TiS_2 and SE during ball-milling is the key to explaining the extra capacity in the BMe samples. The results for the BMe samples were obtained using a weight ratio of TiS_2 to SE of 0.5. This condition might be regarded as unbalanced in terms of energy density based on the total weight of the electrode. For a weight ratio of 1.0 (TiS_2/SE), however, the evolution of the abnormally increased capacity with increased ball milling time is also confirmed, as seen in Figure S4. For example, ball-milling of a 1 : 1 weight ratio of TiS_2 and SE for 27 min resulted in first charge capacities of 442 mA h g^{-1}at 1.5–3.0 V and 909 mA h g^{-1} at 1.0–3.0 V. These capacities are equivalent to 221 mA h (g of electrode)$^{-1}$ and 454 mA h (g of electrode)$^{-1}$, respectively. Note that HMe with even higher weight ratio of TiS_2 to SE of 2.0 produced only 140 mA h (g of electrode)$^{-1}$ (=210 mA h g^{-1}). Therefore, it is fair to say that the controlled ball-milling of TiS_2 and SE together is a viable method for significantly increasing the capacity and energy density of ASSLBs.

In order to analyze the electrochemical behaviors more closely, the voltage curves in Figure 2 are represented by differential capacity plots in Figure 3. As the ball-milling time increases for the 1.5–3.0 V range, it is seen that new reactions between ~1.5 and 1.7 V (denoted as α/α′) and between ~2.3 and 3.0 V (denoted as β/β′) develop. In the case of 1.0–3.0 V, not only the α/α′ and a β/β′ redox

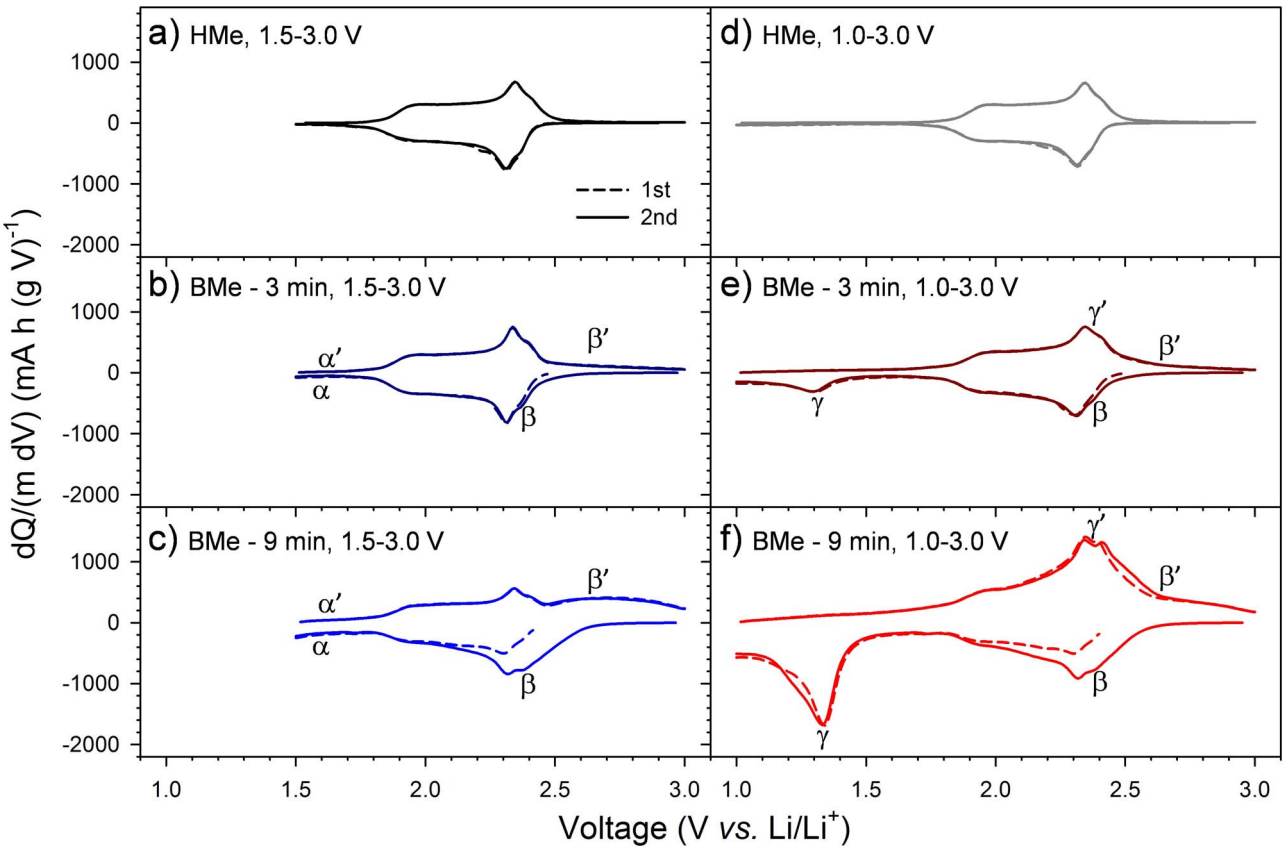

Figure 3 | First two discharge–charge differential voltage profiles of HMe and BMe obtained from the voltage profiles in Figure 2.

couples but also huge redox peaks (denoted as γ/γ′) are added. Overall, comparing HMe and BMe-9-min, it is postulated that the reaction from TiS_2 is overlapped by unknown reactions assigned as α/α′, β/β′, and γ/γ′ that might have originated from the phase formed by a reaction between TiS_2 and SE. Polarization at several states of charge for the first two cycles was recorded by galvanostatic intermittent titration techniques (GITT) and the results are shown in Figure S5. Corresponding well with the differential capacity analyses in Figure 3, relatively larger polarizations (indicated by short dashed circles) are seen in the voltage ranges responsible for α/α′, β/β′, and γ/γ′. This observation implies a very different reaction mechanism for the additional Li^+ storage from the intercalation/deintercalation of Li in TiS_2[30].

In an initial attempt to elucidate the reaction mechanism responsible for the extra capacity of BMe, *ex situ* XRD patterns were obtained and the results are shown in Figure S6. The (001) peak of Li_xTiS_2 is shifted initially from 15.3° to 14.4° by discharge down to 1.5 V and held at the same position down to 1.0 V. Charging up to 3.0 V from 1.5 V and from 1.0 V results in a positive shift, affording a (001) peak at 15.6°, which corresponds well with the peak for fully delithiated TiS_2. However, the XRD patterns obtained do not provide much information about the abnormally increased capacity, implying that the phase responsible for the extra capacity is not crystalline.

A detailed microstructural analysis of the BMe was carried out by HRTEM. An approximately 100-nm-thick specimen of the BMe was prepared by focused ion beam (FIB) sectioning and the results are shown in Figure 4a. An SE region of ~2 μm in size and unique textures surrounding the SE region are seen. The textured region is represented by a dark-field scanning transmission electron microscopy (STEM) image and corresponds to the elemental maps of P and Ti with EDS in Figure 4b. Noticeably, both elements are homogeneously distributed, indicating that TiS_2 may be mixed with SE (Li_3PS_4) on a nanoscale level or that it extensively reacts with SE. From the bright-field TEM image in Figures 4c, it is observed that the unique textures are composed of layered bundles in an amorphous matrix. The HRTEM images in Figures 4d and 4e clearly show the lattice fringes of the layered regions. The spacing is measured to be ~5.8 Å, which matches nicely with the *d* spacing values obtained from the (001) peak of $Li_{0.05}TiS_2$ in BMe in the XRD pattern ($2\theta = 15.3°$, $d = 5.78$ Å) (Figure 1b). The elemental analysis in the amorphous region on the nanoscale level was carried out by EDS, as shown in Figure 4f. Importantly, the amorphous phase includes not only P and S but also Ti. Along with the XRD results in Figure 1b, the elemental analysis by HRTEM with EDS evidences the partial reaction between TiS_2 and Li_3PS_4 SE during ball-milling. The different composition in the two regions in Figure 4f ($Li_xTi_{1.00}P_{1.34}S_{3.88}$ and $Li_yTi_{1.00}P_{1.14}S_{2.47}$), however, indicates inhomogeneity of the partial reaction. It is not surprising that the ball-milling condition is controlled so that not all of the TiS_2 and Li_3PS_4 SE are consumed.

The amorphous Li-Ti-P-S phase confirmed by HRTEM with EDS can explain not only the extra capacity but also the couloumbic efficiency of more than 100% of BMe at the first cycle, as observed in Figure 2 and Table 1. The latter shows that lithium in the newly formed product may be extracted in the first charge (delithiation). In an attempt to further identify the amorphous Li-Ti-P-S phase, the *ex situ* Raman spectra at different discharged and charged states were obtained, as revealed in Figure S7. Unfortunately, the results exhibited signatures from Li_xTiS_2[31] and PS_4^{3-}[7] only. Also, it should be noted that any signal related to sulfur-rich Li_yTiS_x, such as Li_yTiS_3 and Li_yTiS_4[32], and sulfur or Li_xS ($0 < x \leq 2$) was not observed. Overall, the inhomogeneous composition of the amorphous Li-Ti-P-S phase (as displayed in Figure 4f), the lack of data from the *ex situ* XRD and Raman experiments along with the extreme diversity of transition-metal thiophosphates[33] and lack of spectroscopic database restrict the clearer identification of the amorphous Li-Ti-P-S phase.

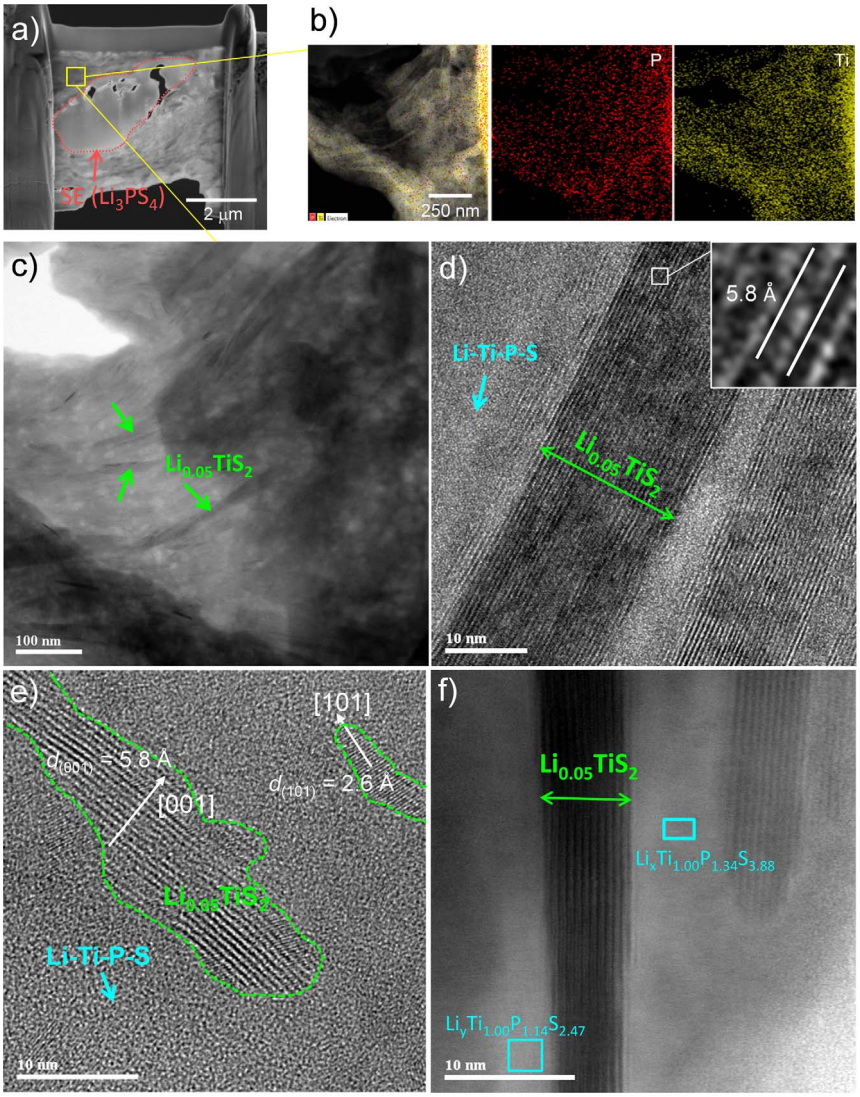

Figure 4 | (a) FESEM image of FIB-sectioned BMe. (b) Dark-field STEM image and corresponding EDS signals of P and Ti of the rectangle region in (a). (c) Bright-field TEM images of the rectangular region in (a). (d and e) HRTEM images of enlarged region in (c). (f) HRTEM image showing the crystalline $Li_{0.05}TiS_2$ and the amorphous region. Chemical compositions of Ti, P, and S of the rectangular regions were obtained by EDS signals.

From the *ex situ* XRD, HRTEM with EDS, and *ex situ* Raman analyses, it is confirmed that the composite electrode comprised crystalline $Li_{0.05}TiS_2$, Li_3PS_4 SE, and amorphous Li-Ti-P-S, which accounts for the unusual extra capacity. As another scenario for the extra capacity, it should not be ruled out that a thin region of Li_3PS_4 SE in contact with the conductive $Li_{0.05}TiS_2$ may be electrochemically activated and participate in additional Li^+ storage. As a control sample, a mixture of nanosized carbon (super P) and SE with a weight ratio of 0.1 (carbon/SE) was ball-milled under the same condition as for BMe (at 2000 rpm for 9 min). Note that carbon will not react with SE, in contrast to the partial reaction between TiS_2 and SE. The first two discharge-charge voltage profiles of the carbon-SE electrode are represented in Figure S8. Very small capacity of 1–2 mA h (g of carbon)$^{-1}$ implies negligible contribution of Li_3PS_4 SE to the abnormally increased capacity.

In order to clarify the mechanism, *ex situ* XPS analysis on the BMe sample was carried out before the cycle and after discharge at 1.5 and 1.0 V. In order to obtain bulk information, the specimens were sputtered with Ar ions for 60 min. The results are represented in Figure 5. As compared to the pristine BMe, the signal of Ti 2p is slightly positively shifted during discharge at 1.5 V. This subtle change agrees with the reference for $TiS_2 + Li^+ + e^- \rightarrow LiTiS_2$[34]. Ti in the amorphous Li-Ti-P-S can also contribute to this change. The signals of P 2p and S 2p remain almost the same after discharge at 1.5 V. In the process of further discharge at 1.0 V, several important changes are highlighted. First, a slightly negative shift of the Ti 2p signal is observed. Second, negative shifts of the signals of both P 2p and S 2p are noticeable. These results present strong evidence that the reduction center in the range 1.0–1.5 V in BMe is not only Ti but also P and S, which is in agreement with the observation from HRTEM with EDS presented in Figures 4d, 4e, and 4f that the amorphous phase includes Ti, P, and S. It was reported that the extra capacity observed in a Chevrel-phase $Cu_xMo_6S_{8-y}$ electrode in ASSLBs at high temperature is related to the diffusion of Cu into the Li_2S–P_2S_5 SE[35]. On a similar basis, some phase formed by a reaction between Cu and SE may be related to the extra capacity as well. The use of $LiTi_2(PS_4)_3$ for lithium-ion battery applications, reported first by Goodenough et al., shows a large capacity in the liquid cell[1,36]. Recently, our group reported that $LiTi_2(PS_4)_3$ in an all-solid-state cell can exhibit a first discharge capacity of ~1050 mA h g^{-1} in 1.2–3.5 V by a conversion reaction[37]. In this context, it is not surprising to learn that a significant contribution to the huge extra capacity occurs by formation of amorphous Li–Ti–P–S phases in BMe in this work. In order to investigate the electrochemical reactivity of the amorphous Li-Ti-

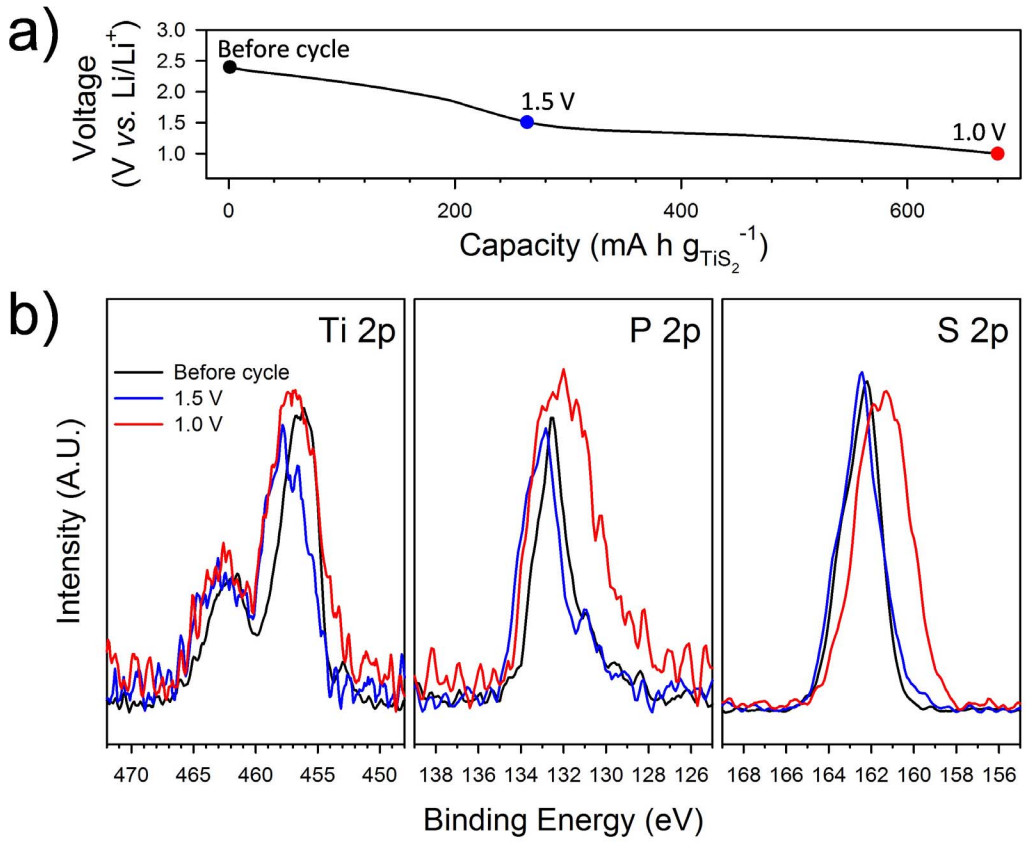

Figure 5 | (a) Discharge voltage curve of the BMe for *ex-situ* XPS experiment. (b) *Ex-situ* XPS results of Ti 2p, P 2p, and S 2p before cycle and after discharge at 1.5 and 1.0 V.

P-S phase in BMe further, two amorphous Li-Ti-P-S powders to mimic the one in the BMe sample were prepared by ball-milling TiS_2 and SE powders until the XRD peaks for TiS_2 and SE disappear as seen in Figure S9a. The amorphous powders prepared from TiS_2 and SE with the weight ratio of 0.5 and 1.0 (TiS_2/SE) were denoted as *a*-BMe1 and *a*-BMe2, respectively. The *a*-BMe1 sample exhibits two orders of magnitude lower electronic conductivity (1.3×10^{-3} S/cm) than that of the BMe sample (7.0×10^{-1} S/cm), which indicates that almost all of TiS_2 might be consumed for the reaction with the SE. In order to examine the electrochemical reactivity of the *a*-BMe samples, the *a*-BMe powders were hand-mixed with the Li_3PS_4 GC SE and conductive carbon additives (*a*-BMe : SE : super P = 20 : 30 : 3 weight ratio), and cycled in the range 1.0–3.0 V. Figure S9b represents the first two discharge-charge voltage profiles. Two features are in common in the electrochemical reactivity of the amorphous phase (*a*-BMe) in Figure S9b and the BMe in Figure 2f (BMe – 9 min). First, two reaction regions at ~2.3 V and ~1.3 V are noticeable in discharge (lithiation). Second, the amount of extracted lithium (charge) exceeds the one of inserted lithium (discharge) at first cycle. From the two common characteristics, it can be postulated that the amorphous powders prepared by the control experiment (*a*-BMe in Figures S9) possibly represent the amorphous Li-Ti-P-S phase in the BMe sample (Figure 2f). Most importantly, the *a*-BMe samples show the abnormally high capacity, which strongly supports that the amorphous Li-Ti-P-S phase in the BMe contributes to the extra capacity.

Figure 6a represents the Nyquist plots of HMe and BMe cells discharged to 2.1 V at the first cycle, which was obtained by electrochemical impedance spectroscopy (EIS). The EIS spectra are composed of R_{SE} at high frequency, which corresponds with the resistance of the SE layer, and Warburg tails at low frequency, which explains Li^+ diffusion into the electrode materials[13]. Importantly, both signals include negligibly small resistance at mid-frequency, which can be assigned to the interfacial charge transfer resistance from TiS_2/SE and Li_xIn/SE. This result highlights an advantageous feature of sulfide-based electrode materials in terms of not only mild operating voltage but also compatibility with sulfide SEs. In sharp contrast, significant charge transfer resistance develops in solid-state cells containing $LiCoO_2$[13]. Also, it is noticeable that both HMe and BMe show similar impedances, which suggests that controlled ball-milling does not degrade the kinetics in composite electrodes. The cycle performances of HMe and BMe at 50 mA g^{-1} are represented in Figure 6b. After 60 cycles, 95% of the initial charge capacity is retained in the range 1.5–3.0 V for both BMe and HMe. The significantly increased capacity of BMe in the range 1.0–3.0 V is offset by deterioration in cycle performance (76% of capacity retention). The large hysteresis in voltage profiles between discharge and charge as seen in Figures 2 and 3 strongly indicates the lithiation reaction in the range 1.0–1.5 V is likely a conversion-type reaction[30,37]. Large volume change and structural reorganization during lithiation-delithiation for the conversion reaction may explain the degradation of BMe cycled in the range 1.0–3.0 V[37]. The charge capacities of HMe and BMe as a function of cycle number with increasing current density in 1.5–3.0 V are represented in Figure 6c. It should be emphasized that the rate performance of BMe is only slightly poorer than that of HMe. This result is in line with the EIS results shown in Figure 6a.

From the XRD results shown in Figure 1b and the FESEM image shown in Figure 4a, it is confirmed that the SE domain is active after ball-milling. In order to evaluate Li^+ ion conduction in the electrode layer, Li^+ ion conductivity was measured using a specially designed electron-blocking symmetric cell of Li/SE/BMe/SE/Li by DC and AC methods (Figure S10). A slightly smaller ionic conductivity for BMe (8.7×10^{-5} S cm^{-1}) than for HMe (1.4×10^{-4} S cm^{-1}) was recorded (Table 2). The electronic conductivities of HMe and BMe pellets

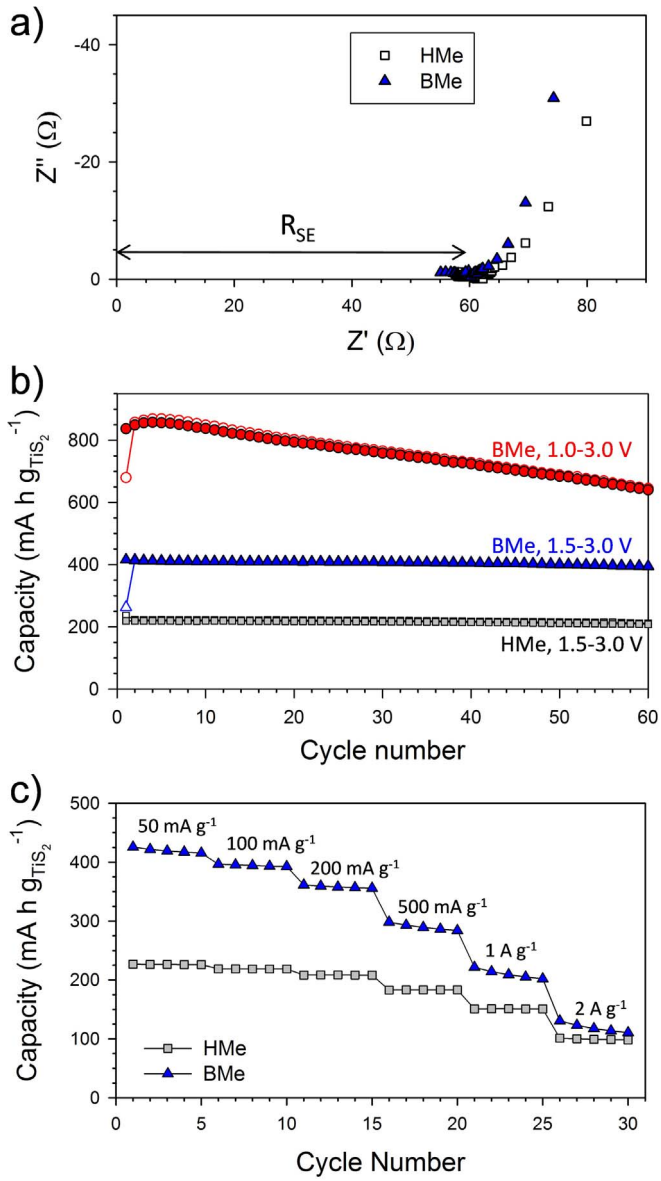

Figure 6 | (a) Nyquist plots of HMe and BMe at first cycle. The R_{SE} term corresponds with the resistance of the SE layer. (b) Cycle performances and (c) rate capabilities of HMe and BMe. The voltage range in c is 1.5–3.0 V. The open and closed symbols in b are discharge and charge capacities, respectively.

measured by the van der Pauw method[38] affords 1.2×10^{1} and 7.0×10^{-1} S cm^{-1}, respectively. The considerably lowered electronic conductivity of BMe also supports the claim that an appreciable amount of the metallic TiS_2 is consumed by the reaction with SE during the controlled ball-milling process. Importantly, however, the electronic conductivity value of 7.0×10^{-1} S cm^{-1} indicates that the remaining Li_xTiS_2 domains in the BMe provide the electronic conduction pathways. These ionic and electronic conductivity measurements demonstrate that the controlled ball-milling of TiS_2 and SE is an effective way to maximize the capacity while maintaining the conduction pathways of the electrode.

Table 2 | Ionic and electronic conductivity of TiS_2–SE composite electrodes

Electrode	Ionic conductivity (S cm^{-1})	Electronic conductivity (S cm^{-1})
TiS_2		2.2×10^{2}
SE	1.0×10^{-3}	1.0×10^{-8}
HMe	1.4×10^{-4}	1.2×10^{1}
BMe	8.7×10^{-5}	7.0×10^{-1}

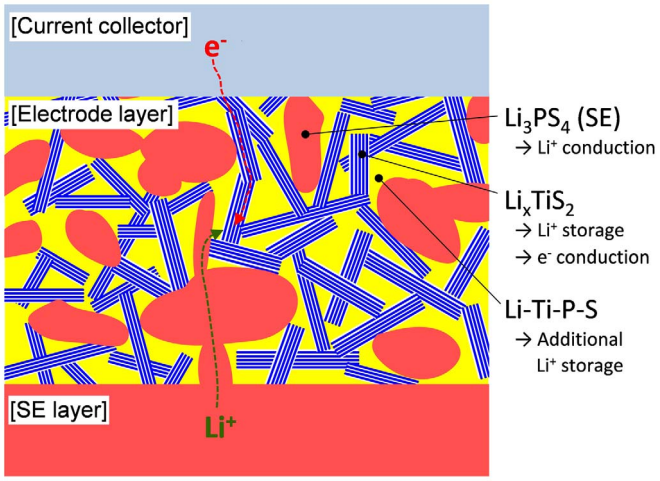

Figure 7 | **Schematic diagram representing the microstructure of BMe in ASSLB.** Electron and Li^+ ion conduction is shown. The role of each component is explained in the figure.

From all the results and analyses so far, a schematic diagram representing the microstructure of BMe and the role of each component is depicted in Figure 7. The controlled ball-milling of TiS_2 and SE can not only downsize the particles and make intimate contacts between TiS_2 and SE, but it also produces amorphous phases of Li–Ti–P–S that contributes to the abnormally increased capacity while retaining ionic and electronic conduction pathways. This strategy can be effectively employed to other electrode systems for ASSLBs.

In conclusion, the controlled ball-milling of a sulfide-active material (TiS_2) and an SE (Li_2S–P_2S_5) for the electrode was demonstrated to achieve considerably increased capacity in ASSLBs without loss of the ionic and electronic conduction pathways. The ball-milled electrode exhibited the first charge capacity of 416 mA h g^{-1} in 1.5–3.0 V at 50 mA g^{-1} at 30°C, with excellent capacity retention of 95% after 60 cycles. The capacity was further increased to ~840 mA h g^{-1} in 1.0–3.0 V offset with a somewhat poorer cycle performance. The origin of the abnormally increased Li^+ storage appeared to be associated with the formation of an amorphous Li–Ti–P–S phase during the controlled ball-milling process. We believe that these results are important in understanding the interfacial phenomena and in the development of high-performance ASSLBs.

Methods

Preparation of Li_2S–P_2S_5 SE. $75Li_2S$–$25P_2S_5$ (or Li_3PS_4) glass-ceramic SE powders were prepared by mechanical milling and subsequent heat treatment. A mixture of 2 g each of Li_2S (99.9%, Alfa Aesar) and P_2S_5 (99%, Sigma Aldrich) were mechanically milled at 500 rpm (8.3 s^{-1}) for 10 h at room temperature using a planetary ball mill (Pulverisette 7PL; Fritsch GmbH) with a ZrO_2 vial (80 mL) and 115 g of ZrO_2 balls (5 mm in diameter). The obtained glass powders were put into a glass ampoule and sealed under vacuum (≤40 Pa). The sealed ampoule was subjected to heat treatment at 243°C for 1 h. Measurements by a Li^+ ion blocking cell (Ti/SE/Ti) with AC and a Li^+ ion non-blocking cell (Li/SE/Li) with DC afforded an ionic conductivity of 1.0×10^{-3} S cm^{-1} at 30°C.

All-solid-state cells. Composite electrode materials were prepared by manually mixing the TiS_2 and SE powders (denoted as HMe) or by ball-milling 30 mg of a TiS_2/SE mixture using a Thinky Mixer (AR-100, THINKY Inc.) with a plastic vial (50 mL) and three ZrO_2 balls (5 mm in diameter) at 2000 rpm (33 s^{-1}, denoted as BMe) for 9 min. The weight ratio of the TiS_2/SE was 0.5. Partially lithiated indium ($Li_{0.5}In$, nominal composition) powders prepared by mixing In (Aldrich, 99%) and Li (FMC Lithium Corp.) powders were used as the counter and reference electrodes. SE pellets were formed by pressing 150 mg of the $75Li_2S$–$25P_2S_5$ glass-ceramic SE at 74 MPa. TiS_2 composite electrode materials (5 mg) were then carefully spread on the top of the SE layer and the cell was pelletized by pressing at 370 MPa for 3 min. Finally, 100 mg

of the prepared $Li_{0.5}In$ powders were attached to the back SE face at 370 MPa for 3 min. All pressings were carried out in a polyaryletheretherketone (PEEK) mold (diameter = 1.3 cm) with Ti metal rods as current collectors for both the working and counter/reference electrodes. All the processes for preparing the SEs and fabricating the all-solid-state cells were performed in an Ar-filled dry box. The galvanostatic discharge–charge cycling of the all-solid-state cells was performed at 50 mA g^{-1} at 30°C. The capacity is based on the weight of TiS_2. The EIS study was performed using an Iviumstat (IVIUM Technologies Corp.). The AC impedance measurements were recorded using a signal with an amplitude of 10 mV and a frequency range from 500 kHz to 5 mHz. The cells were discharged to 2.1 V (vs. Li/Li^+) at 50 mA g^{-1} and a constant voltage of 1.8 V was applied until the current decreased to 10 mA g^{-1}. Then, the cell was allowed to rest for approximately 3 h.

Characterization of materials. For the XRD analyses, a specially designed cell was used, in which the air-sensitive materials such as the TiS_2–SE electrode powders or disassembled all-solid-state cell pellets were placed on a beryllium window and hermetically sealed inside the Ar-filled dry box. Then, the prepared XRD cell was mounted on a D8-Bruker Advance diffractometer equipped with Cu K_α radiation (1.54056 Å). All the XRD patterns were recorded at 40 kV and 40 mA using a continuous scanning mode at 1.5° min^{-1}. For the HRTEM and EDS analyses, the TiS_2–SE electrode pellet was sectioned by using a 30 keV Ga^+ ion beam. A cross-sectional sample with dimensions of $5 \times 5 \times 0.1$ μm^3 was recovered by the lift-out technique and then attached to the Cu TEM grid using a manipulating probe (Copper 3-Post, Omniprobe). Further thinning of the lift-out sample was performed by milling parallel to the cross-sectional plane with low ion beam currents (47 pA) until a final sample thickness of 80–100 nm was achieved. The HRTEM images and EDS elemental mapping were obtained using JEM-2100F (JEOL) with 200 kV and 0.105 mA. For the *ex situ* XPS measurements, the electrode samples collected by disassembling the all-solid-state cells in an Ar-filled dry box were directly transferred to another Ar-filled dry box connected to the XPS equipment (SIGMA PROBE, Thermo Scientific Inc.) without any exposure to air. Characterization with *ex situ* XPS was performed with a monochromatic Al K_α source (1486.6 eV), 100 W, 15 kV, and 6.7 mA. The base pressure in the XPS analysis chamber was less than 1×10^{-7} Pa. XPS spectra were collected using a constant analyzer energy mode with a pass energy value between 30 eV. The step size was 0.1 eV.

1. Goodenough, J. B. & Kim, Y. Challenges for Rechargeable Li Batteries. *Chem. Mater.* **22**, 587–603 (2010).
2. Kamaya, N. *et al.* A lithium superionic conductor. *Nat. Mater.* **10**, 682–686 (2011).
3. Hayashi, A., Noi, K., Sakuda, A. & Tatsumisago, M. Superionic glass-ceramic electrolytes for room-temperature rechargeable sodium batteries. *Nat. Commun.* **3**, 856 (2012).
4. Tarascon, J.-M. Key challenges in future Li-battery research. *Phil. Trans. R. Soc. A* **368**, 3227–3241 (2010).
5. Shimizu, N. Toyota Prototypes All-solid-state Battery With 5× Higher Output Density. http://techon.nikkeibp.co.jp/english/NEWS_EN/20120926/241911/, (2012) date of acess: 10/06/2014.
6. Kanno, R. & Murayama, M. Lithium Ionic Conductor Thio-LISICON. *J. Electrochem. Soc.* **148**, A742–A746 (2001).
7. Mizuno, F., Hayashi, A., Tadanaga, K. & Tatsumisago, M. New, Highly Ion-Conductive Crystals Precipitated from Li_2S-P_2S_5 Glasses. *Adv. Mater.* **17**, 918–921 (2005).
8. Sakuda, A., Hayashi, A. & Tatsumisago, M. Sulfide Solid Electrolyte with Favorable Mechanical Property for All-Solid-State Lithium Battery. *Sci. Reports* **3**, 2261 (2013).
9. Murugan, R., Thangadurai, V. & Weppner, W. Fast Lithium Ion Conduction in Garnet-Type $Li_7La_3Zr_2O_{12}$. *Angew. Chem. Int. Ed.* **46**, 7778–7781 (2007).
10. Kim, K. H. *et al.* Characterization of the interface between $LiCoO_2$ and $Li_7La_3Zr_2O_{12}$ in an all-solid-state rechargeable lithium battery. *J. Power Sources* **196**, 764–767 (2011).
11. Kotobuki, M., Munakata, H., Kanamura, K., Sato, Y. & Yoshida, T. Compatibility of $Li_7La_3Zr_2O_{12}$ Solid Electrolyte to All-Solid-State Battery Using Li Metal Anode. *J. Electrochem. Soc.* **157**, A1076–A1079 (2010).
12. Ohta, N. *et al.* Enhancement of the high-rate capability of solid-state lithium batteries by nanoscale interfacial modification. *Adv. Mater.* **18**, 2226–2229 (2006).
13. Sakuda, A., Kitaura, H., Hayashi, A., Tadanaga, K. & Tatsumisago, M. Modification of Interface Between $LiCoO_2$ Electrode and Li_2S-P_2S_5 Solid Electrolyte Using Li_2O-SiO_2 Glassy Layers. *J. Electrochem. Soc.* **156**, A27–A32 (2009).
14. Woo, J. H. *et al.* Nanoscale Interface Modification of $LiCoO_2$ by Al_2O_3 Atomic Layer Deposition for Solid-State Li Batteries. *J. Electrochem. Soc.* **159**, A1120–A1124 (2012).
15. Trevey, J. E., Jung, Y. S. & Lee, S.-H. High lithium ion conducting Li_2S–GeS_2–P_2S_5 glass–ceramic solid electrolyte with sulfur additive for all solid-state lithium secondary batteries. *Electrochim. Acta* **56**, 4243–4247 (2011).
16. Sakuda, A., Hayashi, A. & Tatsumisago, M. Interfacial Observation between $LiCoO_2$ Electrode and Li_2S-P_2S_5 Solid Electrolytes of All-Solid-State Lithium Secondary Batteries Using Transmission Electron Microscopy. *Chem. Mater.* **22**, 949–956 (2010).
17. Sakuda, A., Hayashi, A., Ohtomo, T., Hama, S. & Tatsumisago, M. $LiCoO_2$ Electrode Particles Coated With Li_2S-P_2S_5 Solid Electrolyte for All-Solid-State Batteries. *Electrochem. Solid-State Lett.* **13**, A73–A75 (2010).
18. Ji, X. L., Lee, K. T. & Nazar, L. F. A highly ordered nanostructured carbon-sulphur cathode for lithium-sulphur batteries. *Nat. Mater.* **8**, 500–506 (2009).
19. Manthiram, A., Fu, Y. & Su, Y.-S. Challenges and Prospects of Lithium-Sulfur Batteries. *Acc. Chem. Res.* **46**, 1125–1134 (2013).
20. Nagao, M., Hayashi, A. & Tatsumisago, M. High-capacity Li_2S–nanocarbon composite electrode for all-solid-state rechargeable lithium batteries. *J. Mater. Chem.* **22**, 10015–10020 (2012).
21. Lin, Z., Liu, Z., Dudney, N. J. & Liang, C. Lithium Superionic Sulfide Cathode for All-Solid LithiumSulfur Batteries. *ACS Nano* **7**, 2829–2833 (2013).
22. Whittingham, M. S. Electrical Energy Storage and Intercalation Chemistry. *Science* **192**, 1126–1127 (1976).
23. Whittingham, M. S. Lithium Batteries and Cathode Materials. *Chem. Rev.* **104**, 4271–4301 (2004).
24. Kim, Y. & Goodenough, J. B. Reinvestigation of $Li_{1-x}Ti_yV_{1-y}S_2$ Electrodes in Suitable Electrolyte: Highly Improved Electrochemical Properties. *Electrochem. Solid-State Lett.* **12**, A73–A75 (2009).
25. Trevey, J. E., Stoldt, C. R. & Lee, S.-H. High Power Nanocomposite TiS_2 Cathodes for All-Solid-State Lithium Batteries. *J. Electrochem. Soc.* **158**, A1282–A1289 (2011).
26. Yersak, T. A., Yan, Y., Stoldt, C. & Lee, S.-H. Ambient Temperature and Pressure Mechanochemical Preparation of Nano-$LiTiS_2$. *ECS Electrochem. Lett.* **1**, A21–A23 (2012).
27. Krawitz, A. D. *Introduction to Diffraction in Materials Science and Engineering*, Wiley: New York, 2001.
28. Chen, J., Tho, Z. L. & Li, S. L. Lithium intercalation in open-ended TiS_2 nanotubes. *Angew. Chem. Int. Ed.* **42**, 2147–2151 (2003).
29. Yersak, T. A., Trevey, J. E. & Lee, S. H. In situ lithiation of TiS_2 enabled by spontaneous decomposition of Li_3N. *J. Power Sources* **196**, 9830–9834 (2011).
30. Ku, J. H., Jung, Y. S., Lee, K. T., Kim, C. H. & Oh, S. M. Thermoelectrochemically Activated MoO_2 Powder Electrode for Lithium Secondary Batteries. *J. Electrochem. Soc.* **156**, A688–A693 (2009).
31. Sandoval, S. J., Chen, X. K. & Irwin, J. C. Raman spectra of Ag_xTiS_2 and lattice dynamics of TiS_2. *Phys. Rev. B* **45**, 14347–14353 (1992).
32. Sakuda, A. *et al.* Amorphous TiS_4 positive electrode for lithium-sulfur secondary batteries. *Electrochem. Commun.* **31**, 71–75 (2013).
33. Wu, Y. & Bensch, W. Structural diversity of rare earth and transition metal thiophosphates. *Crystengcomm* **12**, 1003–1015 (2010).
34. Moreau, P., Ouvrard, G., Gressier, P., Ganal, P. & Rouxel, J. Electronic Structures and Charge Transfer in Lithium and Mercury Intercalated Titanium Disulfides. *J. Phys. Chem. Solids* **57**, 1117–1122 (1996).
35. Nagao, M., Kitaura, H., Hayashi, A. & Tatsumisago, M. High Rate Performance, Wide Temperature Operation and Long Cyclability of All-Solid-State Rechargeable Lithium Batteries Using Mo-S Chevrel-Phase Compound. *J. Electrochem. Soc.* **160**, A819–A823 (2013).
36. Kim, Y., Arumugam, N. & Goodenough, J. B. 3D Framework Structure of a New Lithium Thiophosphate, $LiTi_2(PS_4)_3$, as Lithium Insertion Hosts. *Chem. Mater.* **20**, 470–474 (2008).
37. Shin, B. R. & Jung, Y. S. All-solid-state Rechargeable Lithium Batteries Using $LiTi_2(PS_4)_3$ Cathode with Li_2S-P_2S_5 Solid Electrolyte. *J. Electrochem. Soc.* **161**, A154–A159 (2014).
38. Pauw, L. J. v. d. A Method of Measuring the Resistivity and Hall Coefficient on Lamellae of Arbitary Shape. *Philips Tech. Rev.* **20**, 220 (1958).

Acknowledgments

This work was supported by the Energy Efficiency & Resources Program of the Korea Institute of Energy Technology Evaluation and Planning (KETEP) grant funded by the Korea government Ministry of Trade, Industry & Energy (No. 20112010100150), by the BK21 Plus Program (META-material-based Energy Harvest and Storage Technologies, 10Z20130011057) funded by the Ministry of Education (MOE, Korea) and National Research Foundation of Korea (NRF), and by the Future Strategic Fund (1.130019.01) of UNIST (Ulsan National Institute of Science and Technology).

Author contributions

Y.S.J. designed experiments. B.R.S. and Y.J.N. carried out experiments. All authors contributed data analysis and co-wrote the paper. Y.S.J. proposed and supervised the project.

Additional information

Supplementary information accompanies this paper at http://www.nature.com/scientificreports

Competing financial interests: The authors declare no competing financial interests.

How to cite this article: Shin, B.R., Nam, Y.J., Kim, J.W., Lee, Y.-G. & Jung, Y.S. Interfacial Architecture for Extra Li^+ Storage in All-Solid-State Lithium Batteries. *Sci. Rep.* **4**, 5572; DOI:10.1038/srep05572 (2014).